https://doi.org/10.5194/egusphere-2025-2345
Preprint. Discussion started: 25 June 2025

TensorWeave 1.0: Interpolating geophysical tensor fields with spatial neural networks

Akshay V. Kamath[1], Samuel T. Thiele[1], Hernan Ugalde[2], Bill Morris[3], Raimon Tolosana-Delgado[1], Moritz Kirsch[1], and Richard Gloaguen[1]

[1]Helmholtz-Zentrum Dresden-Rossendorf, Helmholtz Institute Freiberg for Resource Technology, 09599 Freiberg, Germany.
[2]DIP Geosciences, Hamilton, ON Canada.
[3]Morris Magnetics Inc., Fonthill, ON Canada.

Correspondence: Akshay V. Kamath (a.kamath@hzdr.de)

Abstract. Tensor fields, as spatial derivatives of scalar or vector potentials, offer powerful insight into subsurface structures in geophysics. However, accurately interpolating these measurements—such as those from full-tensor potential field gradiometry—remains difficult, especially when data are sparse or irregularly sampled. We present a physics-informed spatial neural network that treats tensors according to their nature as derivatives of an underlying scalar field, enabling consistent, high-fidelity interpolation across the entire domain. By leveraging the differentiable nature of neural networks, our method not only honours the physical constraints inherent to potential fields but also reconstructs the scalar and vector fields that generate the observed tensors. We demonstrate the approach on synthetic gravity gradiometry data and real full-tensor magnetic data from Geyer, Germany. Results show significant improvements in interpolation accuracy, structural continuity, and uncertainty quantification compared to conventional methods.

1 Introduction

Full-tensor gravity and magnetic gradiometry measurements capture the spatial derivatives of potential fields, offering rich detail about subsurface density and magnetization variations. These tensor fields enhance geological imaging by encoding directional and gradient information that scalar fields do not straightforwardly provide (Brewster, 2011; Ugalde et al., 2024). However, gradiometry data are typically sparse and anisotropically sampled—often along sub-parallel flight lines—posing significant challenges for downstream analysis, which relies on gridded representations.

Interpolating these tensor fields accurately is far from trivial. Conventional methods often treat tensor components as independent scalar fields, leading to noise amplification, loss of directional trends, and violations of physical constraints like symmetry and harmonicity. More advanced approaches, such as eigen-decomposition-based interpolation (Satheesh et al., 2023), attempt to preserve tensor structure, but remain limited in generalisability and scalability.

Recent advances in *neural fields*—also known as coordinate-based or implicit neural representations—offer a promising alternative. These models learn continuous functions that map spatial coordinates to field values, and crucially, they are differentiable. This allows them to incorporate gradient information directly into training—a key advantage for geophysical applications where tensor data often represents derivatives of an underlying field (Raissi et al., 2019). However, standard multilayer perceptron (MLP) architectures suffer from spectral bias, meaning they struggle to capture high-frequency features common in geophysical signals (Rahaman et al., 2019). To address this, techniques like random Fourier feature (RFF) mapping and periodic activation functions (e.g., SIREN, Wavelet) have been introduced, enabling neural fields to model fine-scale spatial variations more effectively (Sitzmann et al., 2020; Saragadam et al., 2023).

In this paper, we introduce a physics-informed neural field approach tailored for interpolating geophysical tensor data. Our model learns a single scalar potential field from sparse tensor measurements, leveraging RFF mappings and embedded physical constraints (e.g., symmetry, Laplacian properties) to reconstruct consistent, physically meaningful tensor fields. We further introduce an ensemble strategy to quantify uncertainty in the interpolations, offering insights into data sensitivity and model confidence. We demonstrate this framework on both synthetic gravity data and real airborne magnetic gradiometry from Geyer, Germany, highlighting clear improvements over traditional methods in accuracy and structural continuity, as well as opening the door to uncertainty quantification.

2 Background

A tensor is an algebraic object that encodes multilinear relationships between sets of vectors and linear functionals (Lee, 2012). A tensor field assigns a tensor to every point in space, allowing the local structure of a vector field or scalar potential to be described throughout a region. In geophysical applications, tensors naturally arise as derivatives of vector and scalar fields, extending classical multivariable calculus into field-based formulations.

2.1 Potential fields

Many measured geophysical quantities, such as gravitational acceleration $\boldsymbol{g}$ and the magnetic field $\boldsymbol{b}$, are conservative vector fields—i.e., they are gradients of scalar potential fields (Blakely, 1995). Within $\mathbb{R}^3$, a conservative vector field $\boldsymbol{v}$ is irrotational at all points (given by the position vector $\boldsymbol{r}$), satisfying

$$\boldsymbol{v} = \nabla\phi \quad \leftrightarrow \quad \nabla \times \boldsymbol{v} = 0$$

Where $\nabla = \left[\frac{\partial}{\partial r_x}, \frac{\partial}{\partial r_y}, \frac{\partial}{\partial r_z}\right]$ is the gradient operator. For instance, the magnetic field can be expressed as the gradient of a scalar magnetic potential in regions free of electric currents—a condition typically met outside source distributions. Taking the gradient of $\boldsymbol{v}$ yields the Hessian tensor $\mathbf{H}$, a second-order tensor that captures the local curvature of the scalar potential

$$\mathbf{H} = \nabla\boldsymbol{v} = \nabla(\nabla\phi) = \frac{\partial^2\phi}{\partial r_i \partial r_j} \equiv \partial_i\partial_j\phi \quad \forall\, i,j = 1,2,3$$

In source-free regions, these fields are not only irrotational but also solenoidal—i.e., divergence-free. The divergence of $\boldsymbol{v}$ corresponds to the trace of the Hessian, which reflects the Laplace equation

$$\nabla^2\phi \equiv \mathrm{tr}(\mathbf{H}) = 0$$

This implies that, outside source regions, scalar potentials are harmonic functions, and their Hessians are traceless. Additionally, since mixed partial derivatives commute (by Schwarz's theorem), the Hessians are symmetric and thus comprise five independent components.

2.2 Full Tensor Gradiometry

Direct measurements of second-order Hessian tensors—particularly gravity and magnetic gradient tensors—represent the current frontier in potential field surveying (Rudd et al., 2022; Stolz et al., 2021). Access to the full tensor enables characterization of scalar field curvature, aiding in tasks such as edge detection, structure delineation (Zuo and Hu, 2015), and magnetic remanence characterization (Ugalde et al., 2024). These measurements are typically acquired via airborne surveys, which are highly anisotropic in their sampling: dense along flight lines and sparse across them. Vector fields are frequently reconstructed from tensor components using Fourier-domain transfer functions, which integrate the measured gradients into vector components while suppressing noise (Vassiliou, 1986). Since most downstream analyses, including Fourier-based reconstructions, require gridded tensor and vector fields, interpolation is a critical preprocessing step.

Rudd et al. (2022) note that, in practice, tensor components are often treated as separate scalar fields and interpolated using standard methods like minimum curvature or radial basis functions (RBFs). Several alternative approaches have been proposed to enforce physical or geometric constraints during interpolation. For example, Brewster (2011) uses iterative Fourier-domain transformations, while Fitzgerald et al. (2012) suggest interpolating eigenvalues and eigenvectors separately.

In essence, the quaternion interpolation algorithm decomposes the process into two parts: interpolating the eigenvalues and the corresponding eigenvectors. Two of the three eigenvalues are interpolated using standard schemes (e.g., RBF or minimum

https://doi.org/10.5194/egusphere-2025-2345
Preprint. Discussion started: 25 June 2025

curvature), with the third computed such that their sum is zero—a direct consequence of the Hessian's traceless-ness. The eigenvector matrix of any symmetric real matrix is guaranteed to be real and orthogonal, allowing it to be represented as a 3D orientation and encoded as a quaternion (Hamilton, 1844), provided some constraints on ordering and sign convention are imposed (Satheesh et al., 2023). These quaternions are then interpolated using Spherical Linear Interpolation or SLERP (Shoemake, 1985), which ensures smooth variation of orientation across space. While SLERP works for two quaternions, Markley et al. (2007) devised a scheme that works across a set of weighted quaternions.

However, these methods still have limitations: component-wise methods can be insensitive to the true shape of the tensor, whereas full-tensor schemes involve complex handling of 3D rotations, which are complicated due to the existence of indeterminate points and the need for shifting reference frames due to non-uniqueness of 3D rotations. In this contribution, we propose a neural field method that interpolates the scalar potential field directly—constrained by physical laws and Hessian measurements—to produce consistent, noise-minimizing tensor and vector fields that respect observations and preserve geologically meaningful structures.

2.3 Neural fields

Neural fields—also known as implicit neural representations, or spatial neural networks—are models that represent continuous spatial functions using neural networks. Unlike traditional methods that store information in discrete grids or meshes, neural fields encode spatial structure within the weights and biases of a neural network, enabling resolution-independent, continuous representations of complex signals.

The application of spatial neural networks in geoscience dates back to Openshaw (1993), who used them for interpolating sparse spatial data and found their performance competitive with fuzzy logic and genetic algorithms, a conclusion also reached by Hewitson et al. (1994). More recently, neural fields have gained traction in computer vision—for example, in volumetric radiance field modelling (Mildenhall et al., 2020)—and in geoscience applications such as 3D geological modelling (Hillier et al., 2023) and potential field representation (Smith et al., 2025).

A key advantage of neural fields is their differentiability: they allow access not only to predicted signals but also to their spatial derivatives via automatic differentiation. This is especially useful when the scalar field itself is unobservable or physically arbitrary, but its gradients are measurable—as is often the case in geological modelling using structural orientation data (Kamath et al., 2025; Thiele et al., 2025), or in reconstructing potential fields from tensor gradiometry data.

3 Methodology

This section outlines the key components of our proposed framework, including the use of random Fourier features, a harmonic feature embedding, model architecture, and loss function. We also describe the methodology used to generate the synthetic dataset used in our study.

3.1 Random Fourier Feature mapping

A common challenge in implicit neural representations is the mismatch between low-dimensional input coordinates and the complex, high-frequency structure of the target signal. To address this, we employ *Random Fourier Feature (RFF) mapping*—a kernel approximation technique introduced by Rahimi and Recht (2007) and adapted to deep learning by Tancik et al. (2020). RFF mapping projects spatial coordinates into a higher-dimensional space, making it easier for the network to learn fine-scale spatial variation.

Given the position vector $\boldsymbol{r} \in \mathbb{R}^N$, we define a frequency (also called weights) matrix $\mathbf{W}$, of the dimension $M \times N$, with every component sampled from a standard Gaussian distribution

$$W_{ij} \sim \mathcal{N}(0,1) \tag{1}$$

Where M is the number of Fourier features. Furthermore, to encode known signal frequency characteristics (e.g., the maximum possible frequency based on sampling resolution), we rescale the weights matrix using different length scales. For every length scale $\ell_s \; \forall \; s = 1 \dots L$, we map the position vector onto a $2M$ dimensional feature space, giving us a feature vector $\boldsymbol{\nu}$ with the components given by

$$\nu_i = \sin\left(2\pi \mathbf{W}_s \boldsymbol{r} + \delta_i \frac{\pi}{2}\right) \quad \forall \, i = 1 \dots 2M, \text{ where } \mathbf{W}_s = \frac{\mathbf{W}}{\ell_s}, \; \delta_i = \begin{cases} 0, \; i \text{ is even} \\ 1, \; i \text{ is odd} \end{cases}$$

The transformation enables the model to capture high-frequency details more effectively, while the random sampling of frequencies introduces a useful stochastic component. When followed by a linear MLP with no non-linear activations, the resulting mapping approximates a full Fourier reconstruction of the signal (Bracewell and Kahn, 1966). Non-linear activations help the model fit sparse data more flexibly (LeCun et al., 2015), albeit at the cost of simplicity, interpretability, and gradient stability.

3.2 Harmonic feature embedding

Applying Fourier features uniformly in all dimensions can lead to poor convergence when modelling harmonic functions. Liouville's Theorem (Axler et al., 2001) states that any bounded, periodic, harmonic function in $\mathbb{R}^N$ must be constant. This can cause the network to collapse onto trivial solutions. To avoid this, we partition the position vector into horizontal and vertical components

$$\boldsymbol{r} = \boldsymbol{r}_{xy} + r_z \hat{k} \quad \text{where } \boldsymbol{r}_{xy} \in \mathbb{R}^2$$

We apply the RFF mapping in the horizontal (xy) plane and encode a decaying term in the vertical (z) direction, to replicate the observed decay of scalar potentials and to encourage harmonicity. The modified feature vector $\boldsymbol{\nu}$ therefore has its components given by

$$\nu_i = \sin\left(2\pi \mathbf{W}_s \boldsymbol{r}_{xy} + \delta_i \frac{\pi}{2}\right) \odot e^{-\|\mathbf{W}_s\|_2 r_z} \quad \forall \, i = 1 \dots 2M, \text{ where } \mathbf{W}_s = \frac{\mathbf{W}}{\ell_s}, \; \delta_i = \begin{cases} 0, \; i \text{ is even} \\ 1, \; i \text{ is odd} \end{cases}$$

Where $\mathbf{W}$ is now an $M \times 2$ dimensional weights matrix, $\|\mathbf{W}_s\|_2$ denotes the row-wise Euclidean norm of the weights matrix, and $\odot$ denotes element-wise multiplication. This formulation helps the network respect the expected vertical decay of scalar potentials, aligning the embedding with Laplace's equation. While the network output remains a non-linear combination of the features, this decay-aware encoding enhances generalization in under-sampled regions and theoretically supports upward/downward continuation—though that is outside the scope of this study.

3.3 Synthetic dataset

To evaluate our method, we generated a synthetic gravity gradiometry dataset (Fig. 1) using SimPEG (Cockett et al., 2015). The model consists of three density-contrast anomalies within a zero-density half-space:

1. *Torus*: +1 $\mathrm{g\,cm^{-3}}$, semi-major axis $450\,\mathrm{m}$, semi-minor axis $220\,\mathrm{m}$, cross-section radius $40\,\mathrm{m}$, lying in the xy plane and rotated 12° CCW from the y-axis.
2. *Dyke*: +0.15 $\mathrm{g\,cm^{-3}}$, $60\,\mathrm{m}$ aperture, striking at 45° to the y-axis.
3. *Cube*: –0.2 $\mathrm{g\,cm^{-3}}$, $400\,\mathrm{m}$ side length, rotated 45° about the vertical (z) axis.

The simulation mesh has a voxel size of $20\,\mathrm{m}$. This geometry offers a challenging mix of sharp discontinuities and smooth curvature for testing interpolation. We generated a high-resolution ground truth dataset sampled at $25\,\mathrm{m}$ spacing both along and across the lines, as well as a low-resolution airborne-style dataset with flight lines $200\,\mathrm{m}$ apart in the y direction (perpendicular to the flight line), and sampled densely $(15\,\mathrm{m})$ along the x direction (Fig. 1B-F). Gaussian noise was added to simulate measurement uncertainty.

To test robustness to data sparsity, we also computed 10 versions of the low-resolution dataset with line spacings varying from $80\,\mathrm{m}$ to $560\,\mathrm{m}$. These were used to benchmark interpolation quality and information loss under varying acquisition densities. Comparisons were made with a truncated RBF interpolator (250 nearest neighbours, smoothing factor 100), as well as results from the quaternion interpolation (QUAT, Fitzgerald et al. (2012)), combining RBF-interpolated eigenvalues with SLERP-interpolated quaternions. All results were evaluated on the same high-resolution grid using the R^2 (coefficient of determination), MSE (Mean Squared Error), and SSIM (Structural Similarity Index Measure).

3.4 Model architecture and loss function

Our model has two main components: a RFF mapping block followed by a sequence of fully-connected feed-forward layers that together produce a continuous scalar field representation (Fig. 2. We found that the best performing model for our usage used 64 RFFs and three hidden layers with 1024, 512, and 512 neurons each. The loss function used to train our model involves two types of losses - a data loss and a Laplacian loss. The data loss is computed at the points of measurement between the measured tensor components and the hessians acquired from the predicted scalar field through automatic differentiation (AD) (Margossian, 2019). Since the model is built with pytorch (Paszke et al., 2019), we use the inbuilt `torch.autograd` engine to compute hessians from the scalar field output. For the predicted scalar field , the data loss term is given by

$$\mathcal{L}_d = |\partial_i \partial_j \phi - H_{ij}| \quad \forall\, i,j = 1,2,3$$

Where $\partial_i(\cdot)$ refers to the partial derivative with the respect to the ith input computed with AD, and $\mathbf{H}$ is the measured hessian tensor. Note that this reconstruction loss is computed using all the measurement points.

The second term in the loss function is derived to encourage the predicted scalar field to conform with a partial differential equation defined across the whole domain of interest. Since the predicted field has to be harmonic not only at the points of measurement, but everywhere, we thus penalise non-zero traces of the predicted Hessian tensors, hereafter referred to as the Laplacian loss. During every training epoch, hessians are computed for randomly sampled points within the domain of interest (with the number of points usually set to be equal to the number of measurement points). The Laplacian loss for these predicted tensors is then computed as

$$\mathcal{L}_l = |\mathrm{tr}(\nabla(\nabla\phi))| = |\partial_i \partial_i \phi|$$

Here, the Einstein summation convention is used. This loss penalises high values of the trace of the predicted hessian tensor outside the measured points, thereby encouraging harmonicity on the underlying scalar field within the domain of interest.

When combined, the total loss that is optimised is thus

$$\mathcal{L} = \alpha_d \mathcal{L}_d + \alpha_l \mathcal{L}_l$$

The hyper-parameters α_d and α_l are (optionally) initialised as fractions of the respective initial losses, in order to help find an appropriately balanced weighting of the different loss terms.

3.5 Uncertainty estimation

A key benefit of using RFF embeddings is that their stochastic nature allows for ensemble-based uncertainty estimation. As a result of the stochasticity, each initialisation of the RFF mapping induces a unique basis in the feature space, causing the neural network to converge on a solution that represents a random sample from a broader distribution of plausible scalar fields conditioned on the training data.

To exploit this property for uncertainty quantification, we generate an ensemble of model outputs by varying the random seed used to sample the RFF projection matrix. Ensemble-based uncertainty quantification has a long and successful history in geophysics, particularly in subsurface modelling and inversion. In seismic full waveform inversion (FWI), ensembles have been used to assess the variability and reliability of recovered velocity models under data noise and model ambiguities (Fichtner et al., 2011). In reservoir geophysics, the Ensemble Kalman Filter (EnKF) has become a widely used tool to propagate uncertainty in dynamic reservoir simulation and history matching (Evensen, 2009). More recently, ensemble-based methods have also been applied to probabilistic gravity and magnetotelluric inversion (Laloy et al., 2013), demonstrating their utility in quantifying non-uniqueness and guiding data acquisition strategies.

In our implementation, each ensemble member corresponds to a different realization of the frequency space, leading to stochastically independent function approximations that depend, largely, on the degree to which the solution is constrained by the available data. This ensemble-based approach provides a Monte Carlo-style estimate of the model's epistemic uncertainty. Furthermore, because the scalar field is modelled continuously, we can propagate this ensemble approach to the field's derivatives, helping us quantify uncertainty in derived physical quantities. Therefore, we showcase our results as the Ensemble Neural Field (ENF) method, which corresponds to the average prediction from an ensemble of 100 models.

4 Results

4.1 Synthetic Data

We first evaluate the Ensemble Neural Field (ENF) method on the synthetic gravity gradiometry dataset, comparing it against a Truncated Radial Basis Function (RBF) interpolator (Fig. 3). Panels A and B show the residuals between predicted and true H_{xy} values for the RBF and ENF methods, respectively. The RBF output exhibits high-amplitude residuals (MSE = 4.698 eotvos) between flight lines, indicating overfitting to sampled regions and poor generalisation across them. It also fails to preserve continuity in linear trends that lie at high angles to the flight direction. In contrast, the ENF method yields spatially smoother residuals with significantly lower error (MSE = 0.825 eotvos), suggesting homogeneous improved performance across the domain. Insets in both panels show 1:1 scatter plots, where the ENF predictions cluster more tightly along the identity line—further confirming its accuracy.

Panel C summarises R^2 scores for each tensor component across four interpolation methods: RBF, and two neural field-based (NF and ENF). The NF method reflects the mean R^2 from 100 independently trained models, with error bars showing standard deviation. The ENF method, by contrast, uses the averaged prediction across those same models. Both neural field approaches outperform classical methods, with ENF showing a slight edge—demonstrating that ensemble averaging reduces variance and enhances prediction stability.

To further evaluate structural accuracy, we compute the Structural Similarity Index Measure (SSIM) between predicted and true tensor fields (Fig. 4). The ENF method achieves higher SSIM scores across all three components—0.89 (H_{xx}), 0.90 (H_{xy}), and 0.87 (H_{xz})—compared to 0.79, 0.63, and 0.79 for RBF. The greatest improvement is seen in H_{xy}, where RBF results show structural distortion, over-smoothing, and "boudinage" artefacts along flight lines (Naprstek and Smith, 2019). ENF, on the other hand, preserves coherent anomalies and directional continuity even across sparsely sampled regions.

4.2 Rate of information loss

To assess robustness under sparse sampling, we compare the interpolation results for varying line spacings from $80\,\mathrm{m}$ to $560\,\mathrm{m}$ (Fig. 5). Classical methods (RBF and quaternion-based interpolation, or QUAT) show sharp drops in accuracy beyond $200\,\mathrm{m}$ spacing. For example, the RBF method's average R^2 plummets to 0.43 and SSIM to 0.21 at $560\,\mathrm{m}$. In contrast, NF interpolation maintains relatively stable performance up to $\approx 400\,\mathrm{m}$ spacing, with a much gentler decline at wider gaps. At $560\,\mathrm{m}$, the NF model still achieves an R^2 of 0.87 and an SSIM of 0.58.

The MSE trends mirror this behaviour: classical methods exhibit steep error increases with sparser lines, while the NF model degrades more gracefully. QUAT offers minor improvements over component-wise interpolation but follows a similar performance trajectory. This suggests that the main bottleneck in full tensor interpolation lies in the eigenvalue interpolation step, which—like the component-wise case—relies on RBF methods.

4.3 Magnetic gradiometry from Geyer

Finally, we validated the method on real airborne magnetic gradiometry data from Geyer, located in Germany's Erzgebirge region—part of the Central European Variscides. The area features high- and medium-pressure metamorphic units, orthogneiss domes, and post-orogenic granites (Kroner and Romer, 2013), with abundant ore-forming skarns containing magnetic minerals (Burisch et al., 2019; Lefebvre et al., 2019) as well as magnetite-rich quartzites and amphibolites that occur as intercalations within the metamorphic rocks. These rocks contribute to complex magnetic anomalies ideal for real-world evaluation.

We test the ENF method on a real airborne magnetic gradiometry dataset from Geyer (Fig. 6), acquired by Supracon AG in 2016 as part of the E^3 (ErzExploration Erzgebirge) project. As in the synthetic case, we compare ENF to RBF interpolation. Every fourth flight line is used for training, with the others reserved for validation. Since ground-truth grids are unavailable, we assess accuracy using residual analysis and R^2 scores computed along the withheld lines.

We plot the residual maps for H_{xy} on test lines (Fig. 7). While absolute R^2 scores are lower than in the synthetic case—owing to added geological complexity and noise—ENF still achieves 10–20% better performance than RBF across most tensor components. Residuals show that ENF reduces systematic bias between lines and preserves anomaly shapes more faithfully. RBF, by contrast, displays patchy behaviour with abrupt shifts between lines—a well-known artifact of interpolating sparse or anisotropically sampled data (Hillier et al., 2014; Wittwer, 2009).

To get a qualitative overview of the overall result, we plot the histogram-equalized, gridded visualisations of the H_{xx}, H_{xy}, and H_{xz} tensor components (Fig. 7). Panels A-C show the result from using all of the flight lines with an RBF interpolator, serving as our ground-truth. The RBF results from using every fourth line (Panels D–F) reveal strong aliasing and inconsistent behaviour between flight lines—hallmarks of inadequate cross-line interpolation. In contrast, the ENF interpolations (Panels G–I) exhibit smoother transitions and clearer structural trends, especially in directions orthogonal to flight lines. The ENF model successfully mitigates high-frequency striping and captures geologically meaningful features.

5 Discussion

5.1 Accurately reconstructing tensor fields

The proposed Neural Field (NF) Interpolator has shown remarkable success in interpolating tensor gradiometry data. Our results show that the additional information contained within the hessian tensor can help derive a more accurate reconstruction of the entire field as sampling gets sparser (Fig. 5), provided the interpolation algorithm can access the full tensor constraints. For equivalent inputs, the NF interpolation recovers a signal that better fits all the tensor components, while maintaining the integrability and physical properties inherent to a hessian tensor field.

We also see equivalent results from all methods when line spacings are tight (i.e., for line spacings of $80\,\mathrm{m}$, $100\,\mathrm{m}$ and $120\,\mathrm{m}$ in our synthetic tests). This suggests an oversampling with respect to the spatial frequencies in the signal, such that all the interpolation methods converge to the same (correct) result to yield high accuracy metrics. Results then diverge as line spacing increases to $200\,\mathrm{m}$, indicating the neural field interpolation is able to leverage information in the shape of the tensors to continue to derive accurate reconstructions, while the RBF and quaternion methods cannot.

The reason that the results converge with close spatial sampling could be attributed to the equivalence of SLERP and standard linear interpolation as the angle between the quaternions describing the orientations of the input data points goes to zero. Since a tighter line spacing ensures a smoother graduation of the eigenvector orientations (i.e., a smaller change in the angle between the corresponding quaternions), the resulting interpolation is closer to what one would achieve with standard linear interpolation of the components. But, under sparse sampling conditions, the differences seen in the results indicate that an interpolation using neural field formulation better preserves the shape of interpolated tensors, without the need for cumbersome quaternion formalisms.

The interpolated tensor components for Geyer (Fig. 8) also showcase significant improvements over the component-wise interpolation of these tensors. The extension and continuation of the trend from the centre of the grid, towards the north-east is preserved in the ENF result, but is completely absent in the RBF result. Any interpretation of these grids would thus result in significantly different geological structures, highlighting the necessity for appropriate interpolation methods.

5.2 Recovery of vector fields

Many analysis methods applied to tensor gradiometry data require a domain-wide integral to estimate the underlying vector field. The simplest way of computing this integral is by ignoring everything but the last row of the gradiometry tensor, and using the H_{xz}, H_{yz}, and H_{zz} components to get vector components. Due to the Fourier domain properties, vector components are defined as a vertical integral in the Fourier domain (Mickus and Hinojosa, 2001). Similarly, the power spectrum of these signals can also be used to generate vector components, using transfer functions that fit all of the signals while minimising noise (Vassiliou, 1986). However, in our method, we can completely avoid this potentially complex integral. We can use automatic differentiation to acquire the vector field components from the predicted scalar potential as the neural field predicts scalar

https://doi.org/10.5194/egusphere-2025-2345
Preprint. Discussion started: 25 June 2025

potential and not the gradiometry tensor itself. Importantly, we thus estimate the vector field components exclusively from real measurements, rather than from an integral over a regularly spaced (i.e. interpolated) grid that is already one-step removed from the data.

To test the recovery of vector components from our model, we compared it to the benchmark generated using the RBF interpolation on all flight lines and then applying Fourier domain transfer functions to compute the integral. We also use the transfer functions on the RBF interpolation results for our training data for a baseline comparison (Fig. 9). Comparing the resulting bx (Fig. 9, Panels A, D, and G) components, we see that features present in both the ground truth and the ENF results are completely erased from the RBF result. Similarly, the shape of the anomaly at the top-right corner of the grid is distorted in the RBF result, but completely preserved within the ENF grid. Slight changes in trend directions (i.e., the shift of the strike of the anomalies to having a smaller azimuth) also cannot be seen in the RBF results, which has prominent “boudinage” artefacts along the flight lines that cause a loss of trend and directional information perpendicular to the flight line. We suggest that these results highlight the ability of the neural field interpolation to extract sensible information (resembling the ground truth) from data acquired at four times the line spacing.

5.3 Uncertainty analysis and ensemble models

We also used the stochastic nature of our feature embeddings to do a preliminary uncertainty analysis for the results from our interpolator for the Geyer dataset (Fig. 10). The standard deviation plot shows higher variability in model predictions across regions without data points (i.e., between the flight lines), which could be interpreted as an uncertainty measure. Interestingly, the variance between flight lines seems to scale with the value of the underlying tensor component, leading to heteroscedasticity in the predictions. This might need correction in future developments of our methodology. It is also worth noting that the NF approach has parallels to the turning bands and spectral methods to simulate random fields (Mantoglou and Wilson, 1982), suggesting that a deeper stochastic link to other Gaussian process methods may be possible. This link could be exploited to better understand the variance of neural field ensembles or consider future modifications of the present NF algorithms towards tuned frequency matrix distributions (Equation 1).

The variance of our ensemble model is generally higher for the components with two derivatives in the same dimension (i.e., H_{xx}, H_{yy}, and H_{zz}), and for the derivatives involving the z component (i.e., H_{xy} seems to be the least uncertain). High same-dimension double derivative uncertainties might reflect the propagation of uncertainty through differentiation, as uncertainties in two variables have a chance of cancelling out, but are only amplified with multiple passes through the same derivative operator Li and Oldenburg (1998). The high uncertainty in the z components likely reflects the lack of information in the z direction, as all of our training data are close to coplanar. Furthermore, we also see that the uncertainty in the recovered vector components (Fig. 10, Panels G, H, I) never goes to zero (even where we have measurements of the tensor), reflecting the lack of information on the constant of integration.

5.4 Challenges and future directions

We suggest that the proposed approach opens the door to using neural fields for potential field geophysics, and broader applications involving tensor quantities (e.g., stresses and strains). However, further work and research is needed in several areas. Firstly, our model is highly sensitive to the length scales chosen for the Fourier encoding, and the hyper-parameters of the loss function. This requires a lot of empirical tuning. Automatising hyper-parameter tuning would boost the usability of our method and help to ensure robust results. Furthermore, the inclusion of features with multiple length scales, while tested within our synthetic dataset, needs confirmation for effectiveness in larger areas.

In addition, while the recovery of integrated vector fields is a big advantage of our approach, these have arbitrary integration constants. This ambiguity means that, for every vector component, there is a constant that is unbounded in the other two dimensions. The same problem occurs when we use the Fourier domain transfer functions, as a fundamental lack on long wavelength information leads us to misrepresenting the baseline for the recovered vector field (Ugalde et al., 2024). However, in our methodology, this could be resolved with a few measurements of the vector components included as constraints on the neural field. Therefore, one additional future direction would be to include multiple datasets (e.g., TMI measurements for magnetic gradiometry, satellite or ground gravity measurements for gravity gradiometry) during the training process.

Finally, the inclusion of a harmonic decaying term in the feature mapping makes our method a possible contender for an innovative downward continuation scheme, and thus help with the problem of noise amplification in downward continuation of potential field anomalies. This application needs further research, with proper tuning of the weight matrices and data acquired at multiple elevations for validation.

6 Conclusion

We introduce an innovative Neural Field (NF) interpolation method tailored to tensor gradiometry data in potential field geophysics. This approach leverages the inherent physical relationships among tensor components by representing them as derivatives of an underlying scalar potential field. Our method clearly demonstrates advantages over conventional interpolation techniques, particularly in scenarios involving sparse and anisotropic data coverage, as are typical during aerial surveys.

Our method has shown substantial improvements in interpolation accuracy, structural fidelity, and robustness against data sparsity during evaluations on both synthetic gravity gradiometry data and a real-world magnetic gradiometry dataset from Geyer, Germany. Quantitative comparisons using metrics such as R^2 scores and Structural Similarity Index Measure (SSIM) highlights the NF interpolator's performance across all tensor components, a preservation of geological trends that are typically used during interpretation, and a reduction of common artifacts caused by line-to-line inconsistencies.

Furthermore, by incorporating stochastic random Fourier features, our model likely opens the possibility to quantify uncertainty. Our analysis reveals heteroscedastic behaviour in the interpolations, and also highlights regions that require further data acquisition or refinement. Additionally, our approach seamlessly integrates vector and scalar field reconstructions through automatic differentiation, simplifying subsequent geophysical analyses and interpretations.

Overall, we argue that the proposed NF interpolation method represents a significant advancement in processing tensor gradiometry data. Future developments should focus on larger scale applications, better understanding uncertainty of the model predictions, extended vertical interpolation capabilities (e.g., up- and downward continuations), and the integration of this approach into broader geophysical inversion frameworks.

Acknowledgements. The authors gratefully acknowledge the Federal Institute for Geosciences and Natural Resources (BGR) and Supracon AG for providing the airborne full-tensor magnetic gradiometry dataset from Geyer, acquired in 2016 as part of the E^3 (ErzExploration Erzgebirge) project. This research was supported by funding from the European Union's HORIZON Europe Research Council and UK Research and Innovation (UKRI) under grant agreement No. 101058483 (VECTOR). The authors also thank Vinit Gupta, Ralf Hielscher, and Parth Naik for their valuable insights and constructive discussions, which significantly contributed to improving the clarity and depth of the manuscript.

Code availability. The code used in the study can be found here: https://doi.org/10.5281/zenodo.15480747 (Kamath, 2025); Last access: 21 May, 2025.

Author contributions. AVK: Conceptualization, Formal analysis, Investigation, Methodology, Visualization, Writing – original draft; STT: Conceptualization, Methodology, Writing – original draft, review & editing; HU: Writing – review & editing; BM: Writing – review & editing; RTD: Discussion, Writing - review & editing; MK: Writing – review & editing; RG: Writing – review & editing.

Competing interests. The authors declare that they have no conflict of interest.

https://doi.org/10.5194/egusphere-2025-2345
Preprint. Discussion started: 25 June 2025

References

Axler, S., Bourdon, P., and Ramey, W.: Harmonic Function Theory, vol. 137 of *Graduate Texts in Mathematics*, Springer New York, New York, NY, ISBN 978-1-4419-2911-2 978-1-4757-8137-3, https://doi.org/10.1007/978-1-4757-8137-3, 2001.

Blakely, R. J.: Potential Theory in Gravity and Magnetic Applications, Cambridge University Press, 1 edn., ISBN 978-0-521-41508-8 978-0-521-57547-8 978-0-511-54981-6, https://doi.org/10.1017/CBO9780511549816, 1995.

Bracewell, R. and Kahn, P. B.: The Fourier Transform and Its Applications, American Journal of Physics, 34, 712–712, https://doi.org/10.1119/1.1973431, 1966.

Brewster, J.: Description and evaluation of a full tensor interpolation method, in: SEG Technical Program Expanded Abstracts 2011, pp. 811–814, Society of Exploration Geophysicists, https://doi.org/10.1190/1.3628199, 2011.

Burisch, M., Gerdes, A., Meinert, L. D., Albert, R., Seifert, T., and Gutzmer, J.: The essence of time – fertile skarn formation in the Variscan Orogenic Belt, Earth and Planetary Science Letters, 519, 165–170, https://doi.org/10.1016/j.epsl.2019.05.015, 2019.

Cockett, R., Kang, S., Heagy, L. J., Pidlisecky, A., and Oldenburg, D. W.: SimPEG: An open source framework for simulation and gradient based parameter estimation in geophysical applications, Computers & Geosciences, 85, 142–154, https://doi.org/10.1016/j.cageo.2015.09.015, 2015.

Evensen, G.: Data Assimilation: The Ensemble Kalman Filter, Springer, 2nd edn., 2009.

Fichtner, A., Kennett, B. L. N., Igel, H., and Bunge, H.-P.: Full seismic waveform tomography for upper-mantle structure in the Australasian region using adjoint methods, Geophysical Journal International, 186, 1459–1473, publisher: Oxford University Press, 2011.

Fitzgerald, D., Paterson, R., and Holstein, H.: Comparing Two Methods for Gridding and Honouring Gravity Gradient Tensor Data, Copenhagen, Denmark, https://doi.org/10.3997/2214-4609.20148284, 2012.

Hamilton, W. R.: II. *On quaternions; or on a new system of imaginaries in algebra*, The London, Edinburgh, and Dublin Philosophical Magazine and Journal of Science, 25, 10–13, https://doi.org/10.1080/14786444408644923, 1844.

Hewitson, B. C., Crane, R. G., and Tietze, W., eds.: Neural Nets: Applications in Geography, vol. 29 of *The GeoJournal Library*, Springer Netherlands, Dordrecht, ISBN 978-94-010-4490-5 978-94-011-1122-5, https://doi.org/10.1007/978-94-011-1122-5, 1994.

Hillier, M., Wellmann, F., De Kemp, E. A., Brodaric, B., Schetselaar, E., and Bédard, K.: GeoINR 1.0: an implicit neural network approach to three-dimensional geological modelling, Geoscientific Model Development, 16, 6987–7012, https://doi.org/10.5194/gmd-16-6987-2023, 2023.

Hillier, M. J., Schetselaar, E. M., De Kemp, E. A., and Perron, G.: Three-Dimensional Modelling of Geological Surfaces Using Generalized Interpolation with Radial Basis Functions, Mathematical Geosciences, 46, 931–953, https://doi.org/10.1007/s11004-014-9540-3, 2014.

Kamath, A., Thiele, S., and Gloaguen, R.: (Auto) Differentiating geology: Geological modelling with random Fourier features and neural fields, https://doi.org/10.5194/egusphere-egu25-9746, 2025.

Kamath, A. V.: k4m4th/tensorweave: tensorweave-alpha, https://doi.org/10.5281/ZENODO.15480747, 2025.

Kroner, U. and Romer, R.: Two plates — Many subduction zones: The Variscan orogeny reconsidered, Gondwana Research, 24, 298–329, https://doi.org/10.1016/j.gr.2013.03.001, 2013.

Laloy, E., Vrugt, J. A., Jacques, D., and Mallants, D.: Probabilistic inversion of time-lapse ground-penetrating radar data using Markov chain Monte Carlo and multilayer neural networks, Water Resources Research, 49, 6247–6263, publisher: Wiley Online Library, 2013.

LeCun, Y., Bengio, Y., and Hinton, G.: Deep learning, Nature, 521, 436–444, https://doi.org/10.1038/nature14539, 2015.

Lee, J. M.: Introduction to Smooth Manifolds, vol. 218 of *Graduate Texts in Mathematics*, Springer New York, New York, NY, ISBN 978-1-4419-9981-8 978-1-4419-9982-5, https://doi.org/10.1007/978-1-4419-9982-5, 2012.

https://doi.org/10.5194/egusphere-2025-2345
Preprint. Discussion started: 25 June 2025

Lefebvre, M. G., Romer, R. L., Glodny, J., Kroner, U., and Roscher, M.: The Hämmerlein skarn-hosted polymetallic deposit and the Eibenstock granite associated greisen, western Erzgebirge, Germany: two phases of mineralization—two Sn sources, Mineralium Deposita, 54, 193–216, https://doi.org/10.1007/s00126-018-0830-4, 2019.

Li, Y. and Oldenburg, D. W.: 3-D inversion of gravity data, GEOPHYSICS, 63, 109–119, https://doi.org/10.1190/1.1444302, 1998.

Mantoglou, A. and Wilson, J. L.: The Turning Bands Method for simulation of random fields using line generation by a spectral method, Water Resources Research, 18, 1379–1394, https://doi.org/10.1029/WR018i005p01379, 1982.

Margossian, C. C.: A Review of automatic differentiation and its efficient implementation, https://doi.org/10.1002/WIDM.1305, arXiv:1811.05031 [cs], 2019.

Markley, F. L., Cheng, Y., Crassidis, J. L., and Oshman, Y.: Averaging Quaternions, Journal of Guidance, Control, and Dynamics, 30, 1193–1197, https://doi.org/10.2514/1.28949, 2007.

Mickus, K. L. and Hinojosa, J. H.: The complete gravity gradient tensor derived from the vertical component of gravity: a Fourier transform technique, Journal of Applied Geophysics, 46, 159–174, https://doi.org/10.1016/S0926-9851(01)00031-3, 2001.

Mildenhall, B., Srinivasan, P. P., Tancik, M., Barron, J. T., Ramamoorthi, R., and Ng, R.: NeRF: Representing Scenes as Neural Radiance Fields for View Synthesis, in: Proceedings of the European Conference on Computer Vision (ECCV), pp. 405–421, Springer, 2020.

Naprstek, T. and Smith, R. S.: A new method for interpolating linear features in aeromagnetic data, GEOPHYSICS, 84, JM15–JM24, https://doi.org/10.1190/geo2018-0156.1, 2019.

Openshaw, S.: Modelling spatial interaction using a neural net, in: Geographic Information Systems, Spatial Modelling and Policy Evaluation, edited by Fischer, M. M. and Nijkamp, P., pp. 147–164, Springer Berlin Heidelberg, Berlin, Heidelberg, ISBN 978-3-642-77502-4 978-3-642-77500-0, https://doi.org/10.1007/978-3-642-77500-0_10, 1993.

Paszke, A., Gross, S., Massa, F., Lerer, A., Bradbury, J., Chanan, G., Killeen, T., Lin, Z., Gimelshein, N., Antiga, L., Desmaison, A., Köpf, A., Yang, E., DeVito, Z., Raison, M., Tejani, A., Chilamkurthy, S., Steiner, B., Fang, L., Bai, J., and Chintala, S.: PyTorch: An Imperative Style, High-Performance Deep Learning Library, https://doi.org/10.48550/ARXIV.1912.01703, version Number: 1, 2019.

Rahaman, N., Baratin, A., Arpit, D., Draxler, F., Lin, M., Hamprecht, F. A., Bengio, Y., and Courville, A.: On the Spectral Bias of Neural Networks, in: Proceedings of the 36th International Conference on Machine Learning (ICML), vol. 97 of *Proceedings of Machine Learning Research*, pp. 5301–5310, 2019.

Rahimi, A. and Recht, B.: Random Features for Large-Scale Kernel Machines, in: Advances in Neural Information Processing Systems, edited by Platt, J., Koller, D., Singer, Y., and Roweis, S., vol. 20, Curran Associates, Inc., https://proceedings.neurips.cc/paper_files/paper/2007/file/013a006f03dbc5392effeb8f18fda755-Paper.pdf, 2007.

Raissi, M., Perdikaris, P., and Karniadakis, G. E.: Physics-informed neural networks: A deep learning framework for solving forward and inverse problems involving nonlinear partial differential equations, Journal of Computational Physics, 378, 686–707, https://doi.org/10.1016/j.jcp.2018.10.045, 2019.

Rudd, J., Chubak, G., Larnier, H., Stolz, R., Schiffler, M., Zakosarenko, V., Schneider, M., Schulz, M., and Meyer, M.: Commercial operation of a SQUID-based airborne magnetic gradiometer, The Leading Edge, 41, 486–492, https://doi.org/10.1190/tle41070486.1, 2022.

Saragadam, V., LeJeune, D., Tan, J., Balakrishnan, G., Veeraraghavan, A., and Baraniuk, R. G.: WIRE: Wavelet Implicit Neural Representations, https://doi.org/10.48550/ARXIV.2301.05187, 2023.

Satheesh, A., Schmidt, C. P., Wall, W. A., and Meier, C.: Structure-preserving invariant interpolation schemes for invertible second-order tensors, International Journal for Numerical Methods in Engineering, 125, https://doi.org/10.1002/nme.7373, 2023.

Shoemake, K.: Animating rotation with quaternion curves, ACM SIGGRAPH Computer Graphics, 19, 245–254, https://doi.org/10.1145/325165.325242, 1985.

Sitzmann, V., Martel, J. N. P., Bergman, A. W., Lindell, D. B., and Wetzstein, G.: Implicit Neural Representations with Periodic Activation Functions, CoRR, abs/2006.09661, https://arxiv.org/abs/2006.09661, 2020.

Smith, L. T., Horrocks, T., Akhtar, N., Holden, E.-J., and Wedge, D.: Implicit neural representation for potential field geophysics, Scientific Reports, 15, 9799, https://doi.org/10.1038/s41598-024-83979-z, 2025.

Stolz, R., Schmelz, M., Zakosarenko, V., Foley, C. P., Tanabe, K., Xie, X., and Fagaly, R.: Superconducting sensors and methods in geophysical applications, Superconductor Science and Technology, https://doi.org/10.1088/1361-6668/abd7ce, 2021.

Tancik, M., Srinivasan, P. P., Mildenhall, B., Fridovich-Keil, S., Raghavan, N., Singhal, U., Ramamoorthi, R., Barron, J. T., and Ng, R.: Fourier Features Let Networks Learn High Frequency Functions in Low Dimensional Domains, https://doi.org/10.48550/ARXIV.2006.10739, 2020.

Thiele, S., Kamath, A., and Gloaguen, R.: Less is more: Weakly supervised interpolation using geological neural fields, https://doi.org/10.5194/egusphere-egu25-8735, 2025.

Ugalde, H., Morris, B., Kamath, A., and Parsons, B.: Full-tensor magnetic gradiometry: Comparison with scalar total magnetic intensity, processing and visualization guidelines, Geophysical Prospecting, 73, 303–314, https://doi.org/10.1111/1365-2478.13629, 2024.

Vassiliou, A.: Numerical techniques for processing airborne gradiometer data, https://doi.org/10.11575/PRISM/23539, 1986.

Wittwer, T.: Regional gravity field modeling with radial basis functions, vol. 72 of *Publications on Geodesy*, Nederlandse Commissie voor Geodesie, ISBN 978-90-6132-315-0, https://doi.org/10.54419/hboxky, 2009.

Zuo, B. and Hu, X.: Edge detection of gravity field using eigenvalue analysis of gravity gradient tensor, Journal of Applied Geophysics, 114, 263–270, https://doi.org/10.1016/j.jappgeo.2015.01.013, 2015.

450 **Figures**

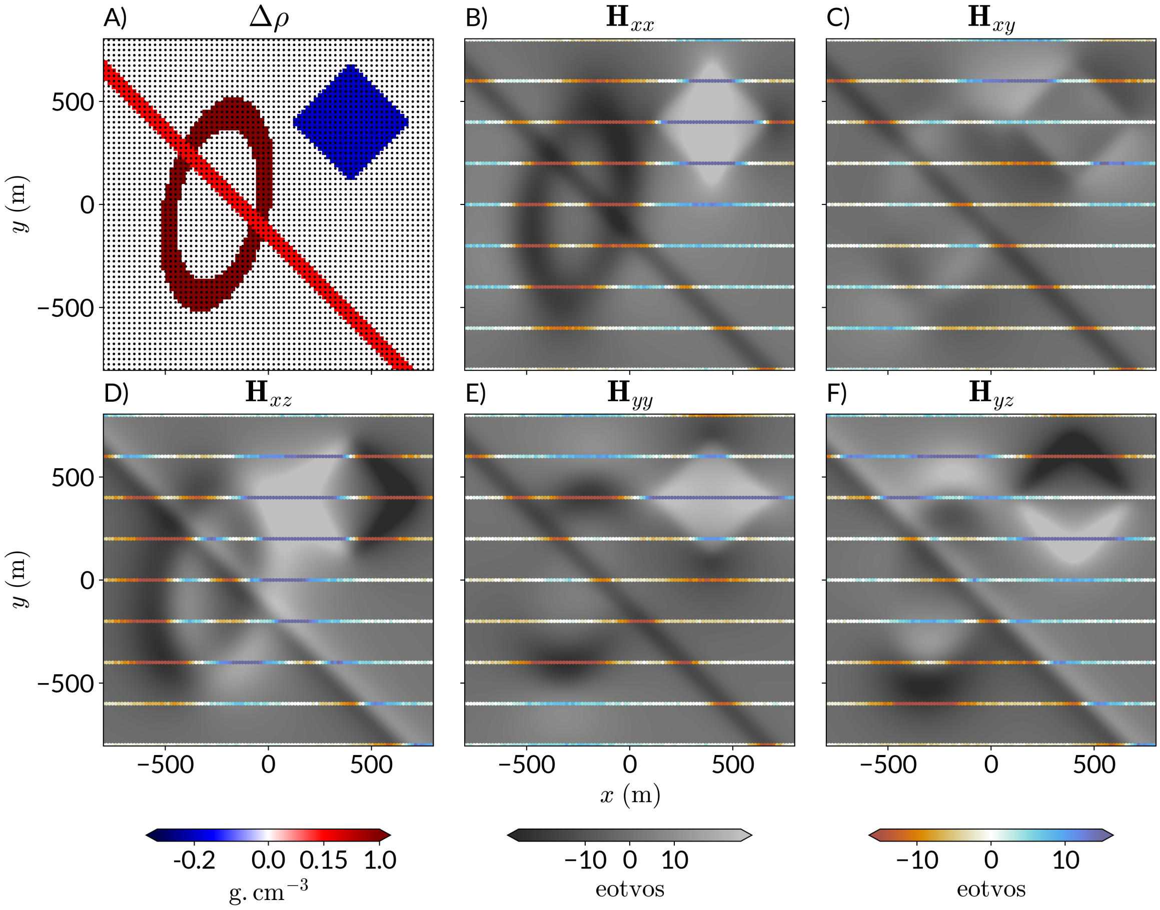

Figure 1. Synthetic subsurface model and corresponding gravity gradiometry data. (A) Horizontal cross-section of the synthetic geological model at a depth of $140\,\mathrm{m}$, with high-resolution observation points shown as black dots. (B–F) The five independent components of the gravity gradiometry tensor generated via forward modelling using SimPEG. Each panel displays both the high-resolution dataset (greyscale; cell size of $25\,\mathrm{m}$) and the low-resolution dataset (colour; $200\,\mathrm{m}$ cross-line spacing and $15\,\mathrm{m}$ inline spacing) for the corresponding tensor component.

https://doi.org/10.5194/egusphere-2025-2345
Preprint. Discussion started: 25 June 2025

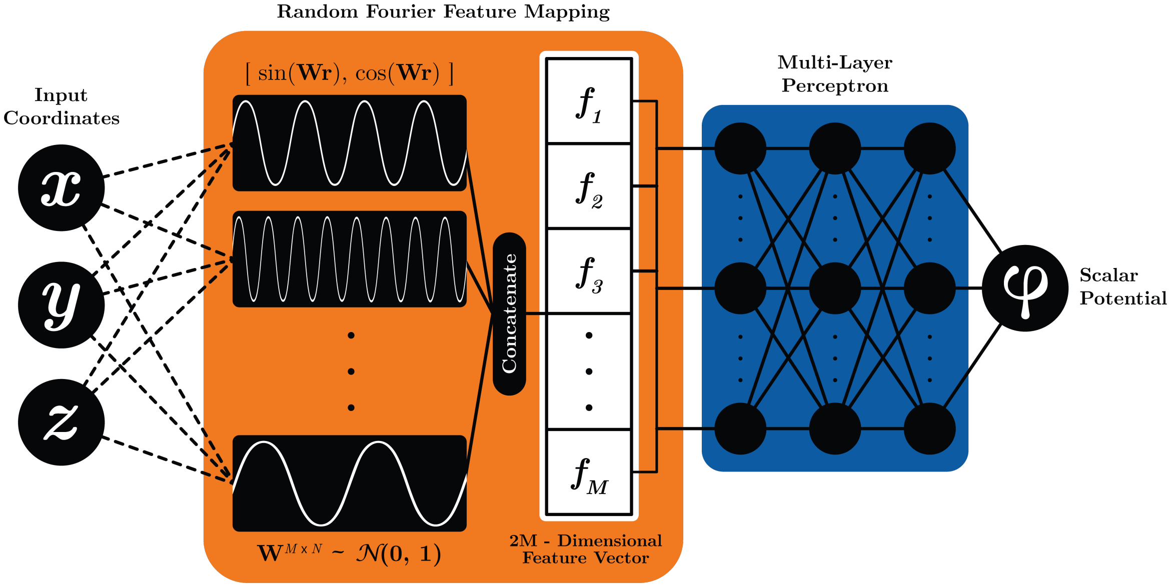

Figure 2. Neural field model architecture. The orange block projects the input position vector into a feature space and passes it through the fully-connected layers to acquire the scalar potential.

https://doi.org/10.5194/egusphere-2025-2345
Preprint. Discussion started: 25 June 2025

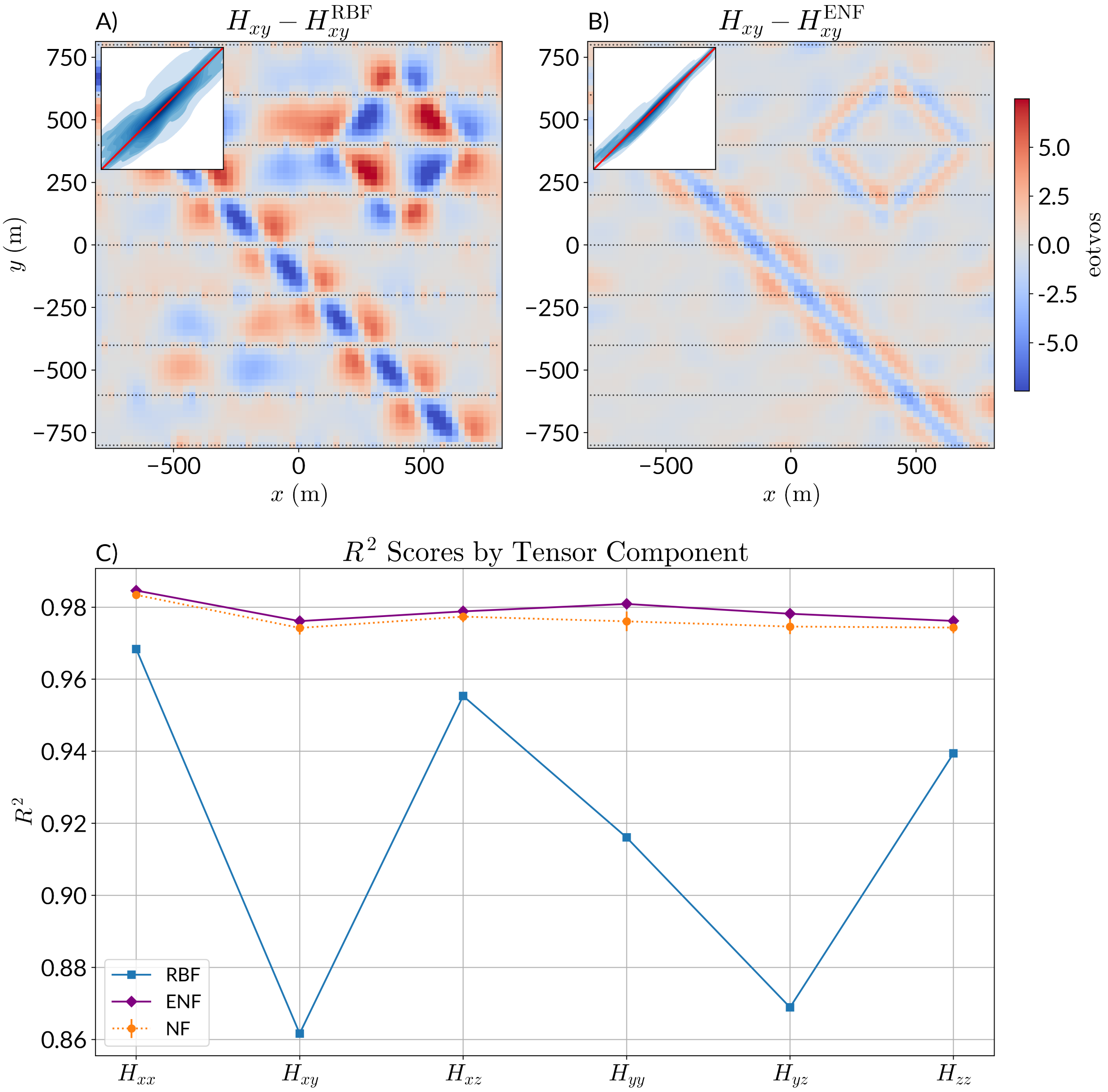

Figure 3. Quantitative comparison of interpolation performance for the synthetic dataset. (A–B) Spatial distribution of residuals between the true and predicted H_{xy} tensor component using (A) the Truncated Radial Basis Function (RBF) method and (B) the Ensemble Neural Field (ENF) approach. Insets show 1:1 parity kernel density estimate plots comparing predicted and true values. (C) R^2 scores for each tensor component (H_{xx}, H_{xy}, H_{xz}, H_{yy}, H_{yz}, H_{zz}) across three interpolation methods: RBF, the mean of the individual Neural Field (NF) scores from the models within the ensemble, and ENF. The ENF and NF models consistently achieve higher accuracy across all components, while RBF exhibits reduced performance, particularly for off-diagonal terms.

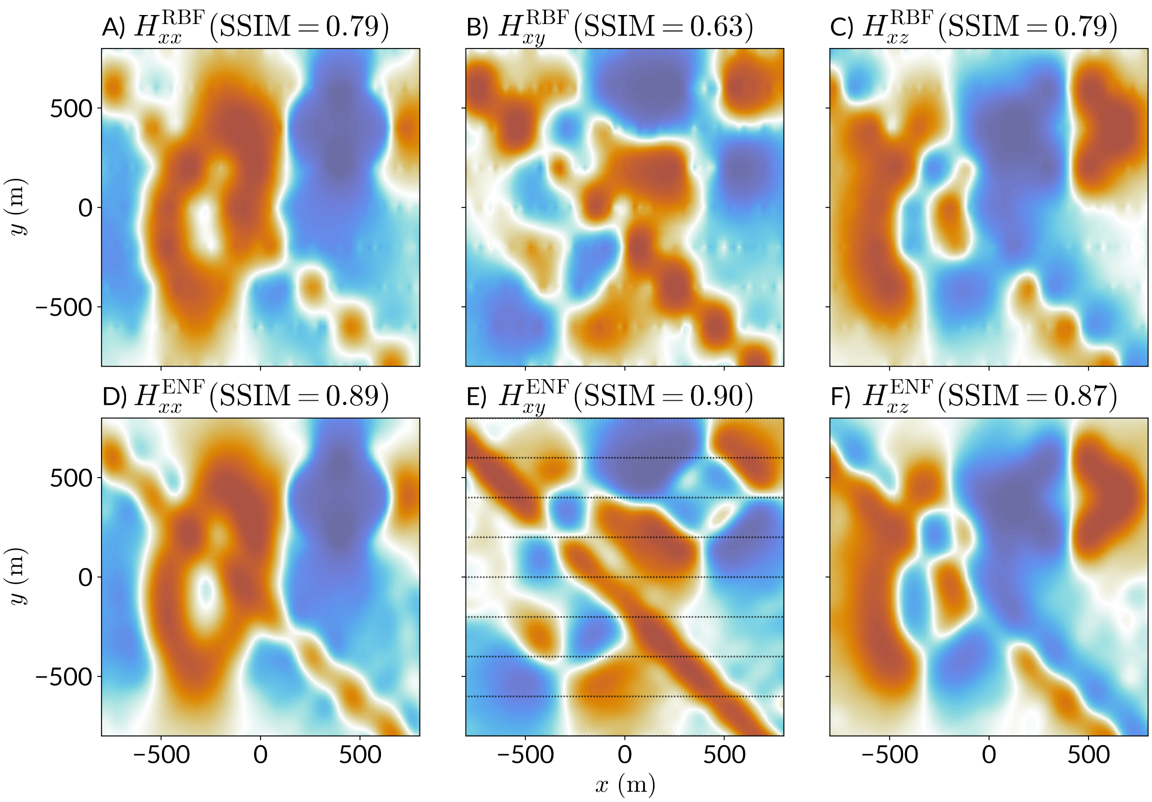

Figure 4. Comparison of gravity gradiometry tensor components derived from two interpolation methods applied to the synthetic dataset. (A–C) Gridded, histogram-equalised H_{xx} , H_{xy} , and H_{xz} components generated using a Truncated Radial Basis Function (RBF) interpolation with 250 nearest neighbours and a smoothing factor of 100. (D–F) Corresponding results produced by the Ensemble Neural Field (ENF) method. All values range from 0 to 1. Black lines in panel (E) indicate the input flight lines used for interpolation.

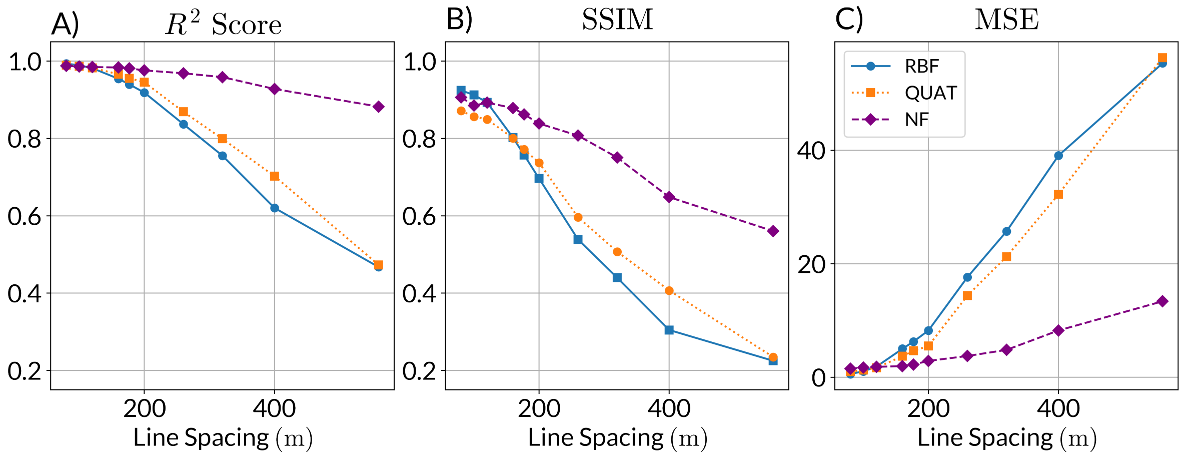

Figure 5. Accuracy metrics as a function of increasing line spacing for the synthetic dataset. (A) R^2 Score and (B) Structural Similarity Index Measure (SSIM) (C) Mean Squared Error (MSE) were computed between the ground truth and the gridded results from the interpolation methods. The Radial Basis Function (RBF) used 250 nearest neighbours, with a smoothing factor of 100, and the Neural Field (NF) model used the same architecture as discussed in Section 3.3. The full tensor interpolation algorithm from Fitzgerald et al. (2012)(QUAT) was also included for comparison, using the aforementioned RBF for the eigenvalue interpolation, and SLERP for rotational interpolation.

https://doi.org/10.5194/egusphere-2025-2345
Preprint. Discussion started: 25 June 2025

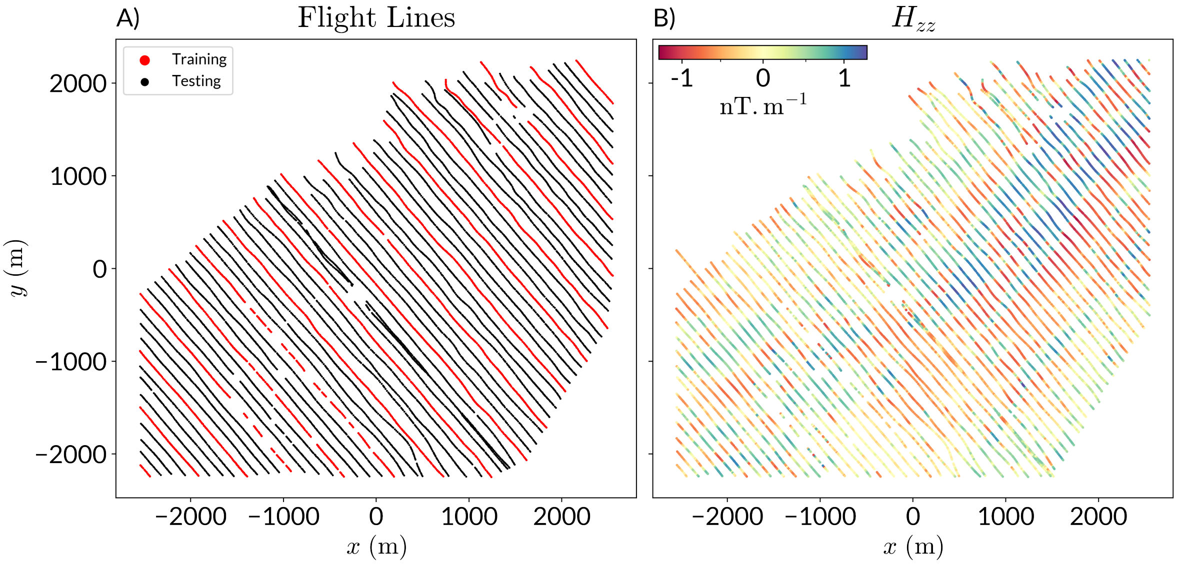

Figure 6. Case study site near Geyer, Erzgebirge, Germany. (A) Flight lines from a subset of the airborne magnetic gradiometry survey, with every fourth line (red) used as input for interpolation and the remaining lines (black) reserved for validation. (B) Spatial distribution of the measured zz-component of the magnetic gradiometry tensor across the survey region.

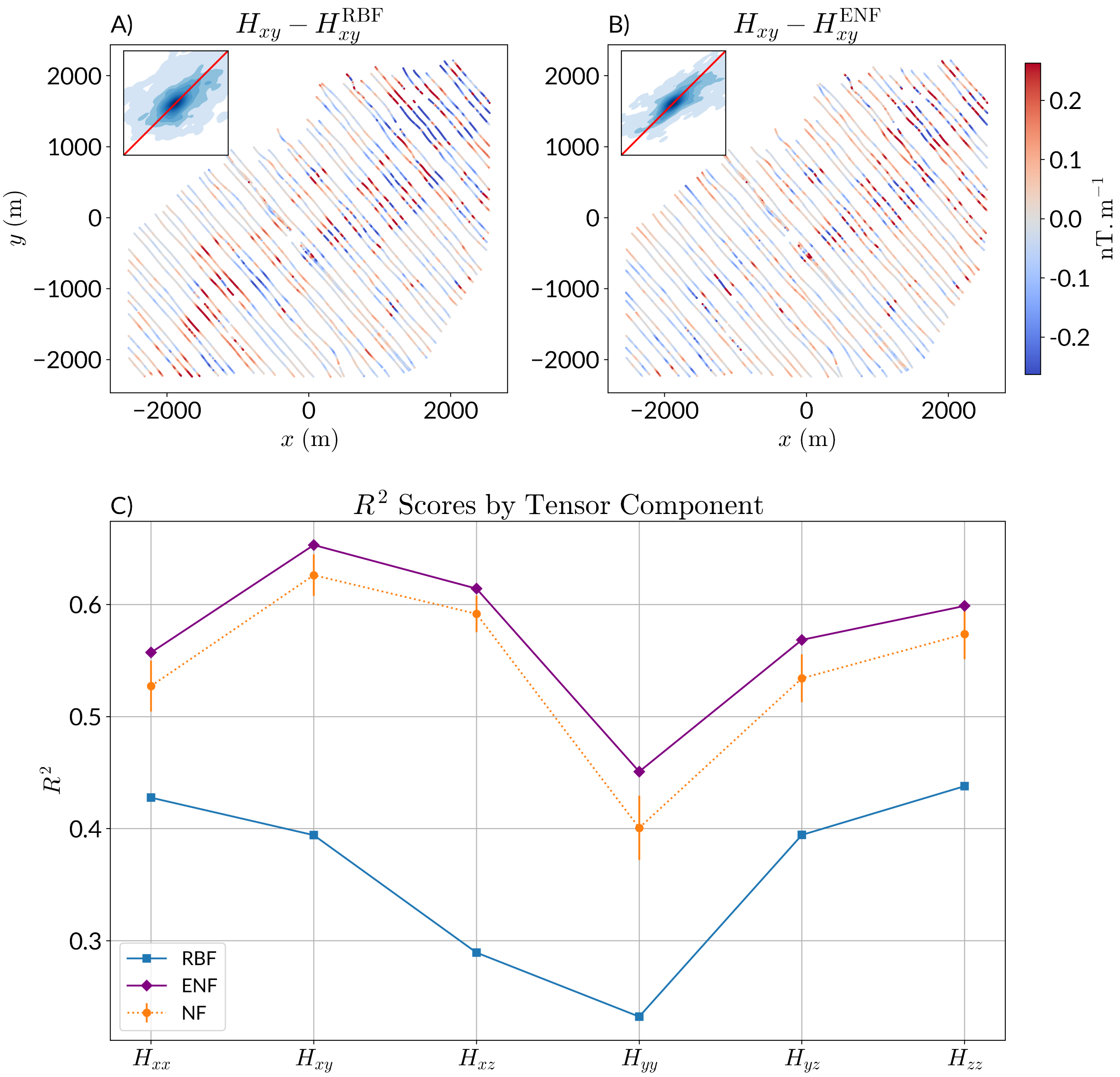

Figure 7. Quantitative comparison of interpolation performance for the Geyer dataset. (A–B) Spatial distribution of residuals between the true and predicted H_{xy} tensor component along the test flight lines using (A) the Truncated Radial Basis Function (RBF) method and (B) the Ensemble Neural Field (ENF) approach. Insets show 1:1 parity kernel density estimate plots comparing predicted and true values. (C) R^2 scores for each tensor component (H_{xx}, H_{xy}, H_{xz}, H_{yy}, H_{yz}, H_{zz}) across three interpolation methods: RBF, mean of the individual Neural Field (NF) scores from the models within the ensemble, and ENF. The ENF and NF models consistently achieve higher scores across all components, while RBF exhibits reduced performance, particularly for off-diagonal terms.

https://doi.org/10.5194/egusphere-2025-2345
Preprint. Discussion started: 25 June 2025

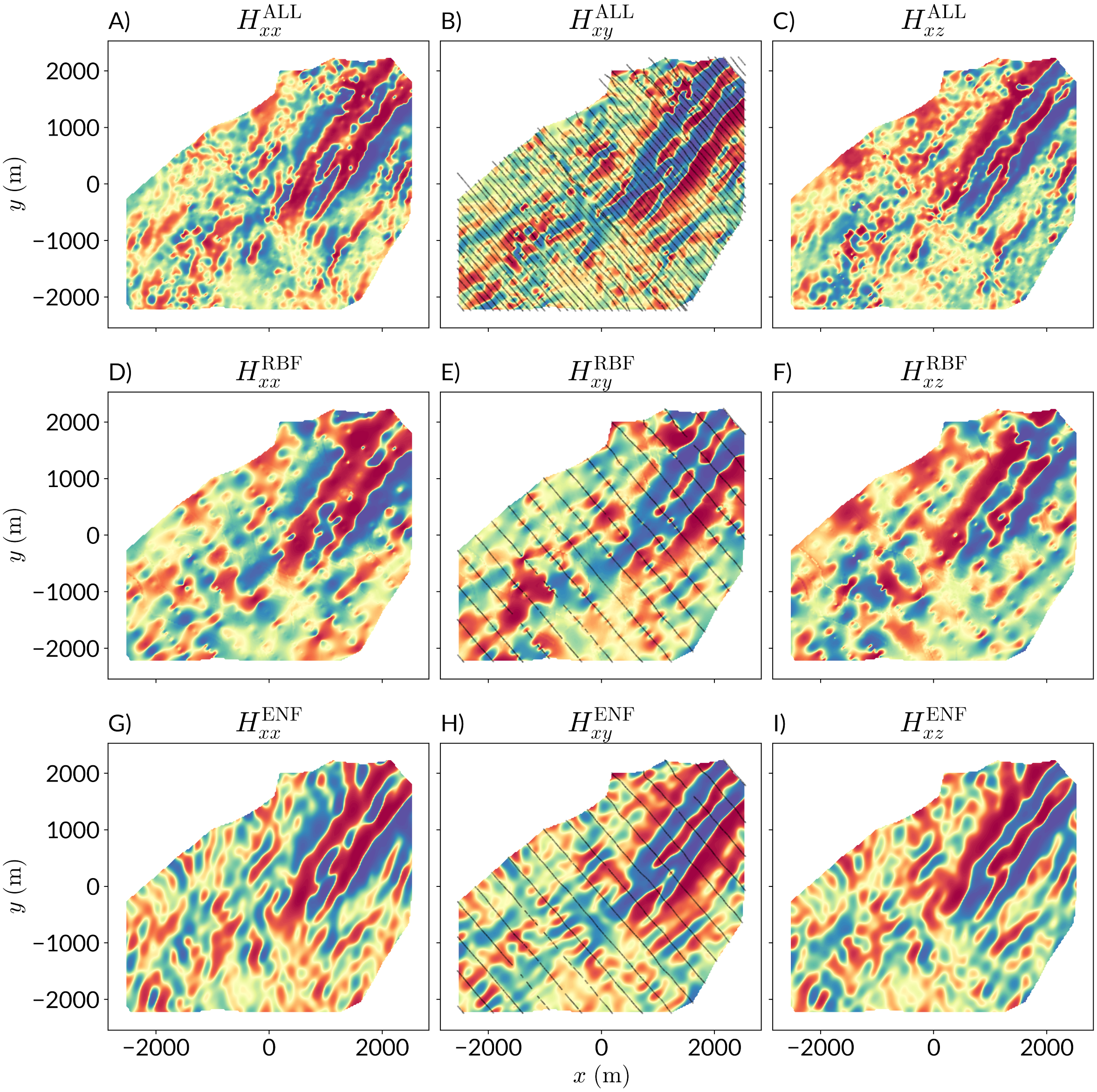

Figure 8. Comparison of magnetic gradient tensor components interpolated onto a uniform grid (cell size $= 25\,\mathrm{m}$) using two methods. (A–C) Gridded, histogram-equalised H_{xx}, H_{xy}, and H_{xz} components obtained using the Truncated Radial Basis Function (RBF) interpolation method, with 250 nearest neighbours and a smoothing factor of 100 for all of the flight lines, (D-F) Corresponding components interpolated with RBF using every fourth flight line, (G-I) Corresponding components interpolated using the Ensemble Neural Field (ENF) approach. Each column visualizes a distinct tensor component of the tensor. All values range from 0 to 1. Black lines in panels B, E and H indicate the locations of the input flight lines used in the interpolation process.

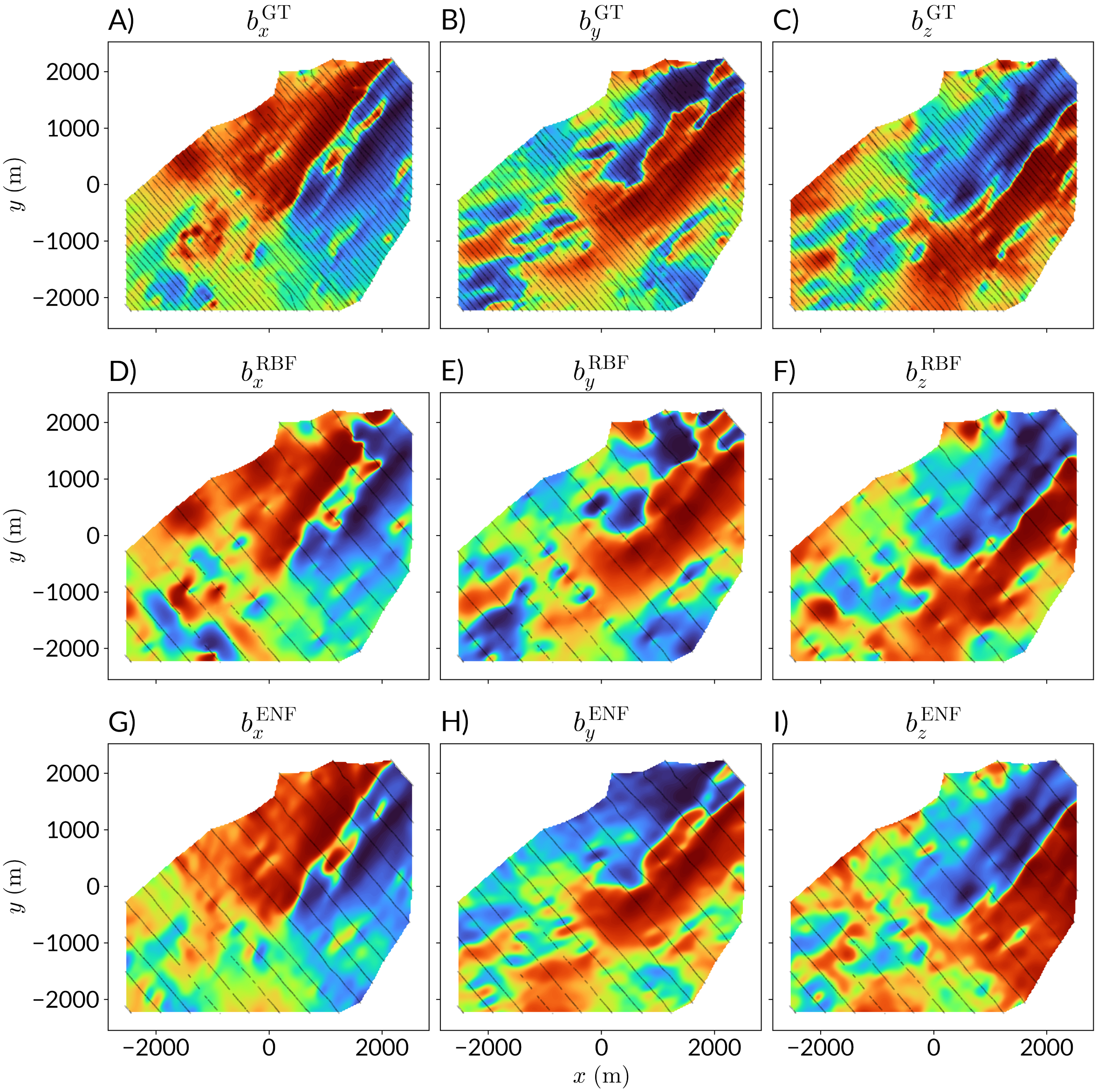

Figure 9. Comparison of recovered vector magnetic field components from two interpolation methods, evaluated against a high-resolution reference model. (A–C) Reference vector components b_x, b_y, and b_z computed using Fourier domain transfer functions applied to magnetic tensor components gridded via the Truncated Radial Basis Function (RBF) from all available flight lines. (D–F) Reconstructed vector components obtained using the RBF method on tensor data from the training set of flight lines. (G–I) Corresponding results computed from the spatial derivatives of the scalar field predicted by the Ensemble Neural Field (ENF) model. The black lines in each panel represent the flight lines used to generate the corresponding component. Each panel shows the histogram-equalised spatial distribution of the respective vector component across the subset of the Geyer survey area, mapped from 0 to 1.

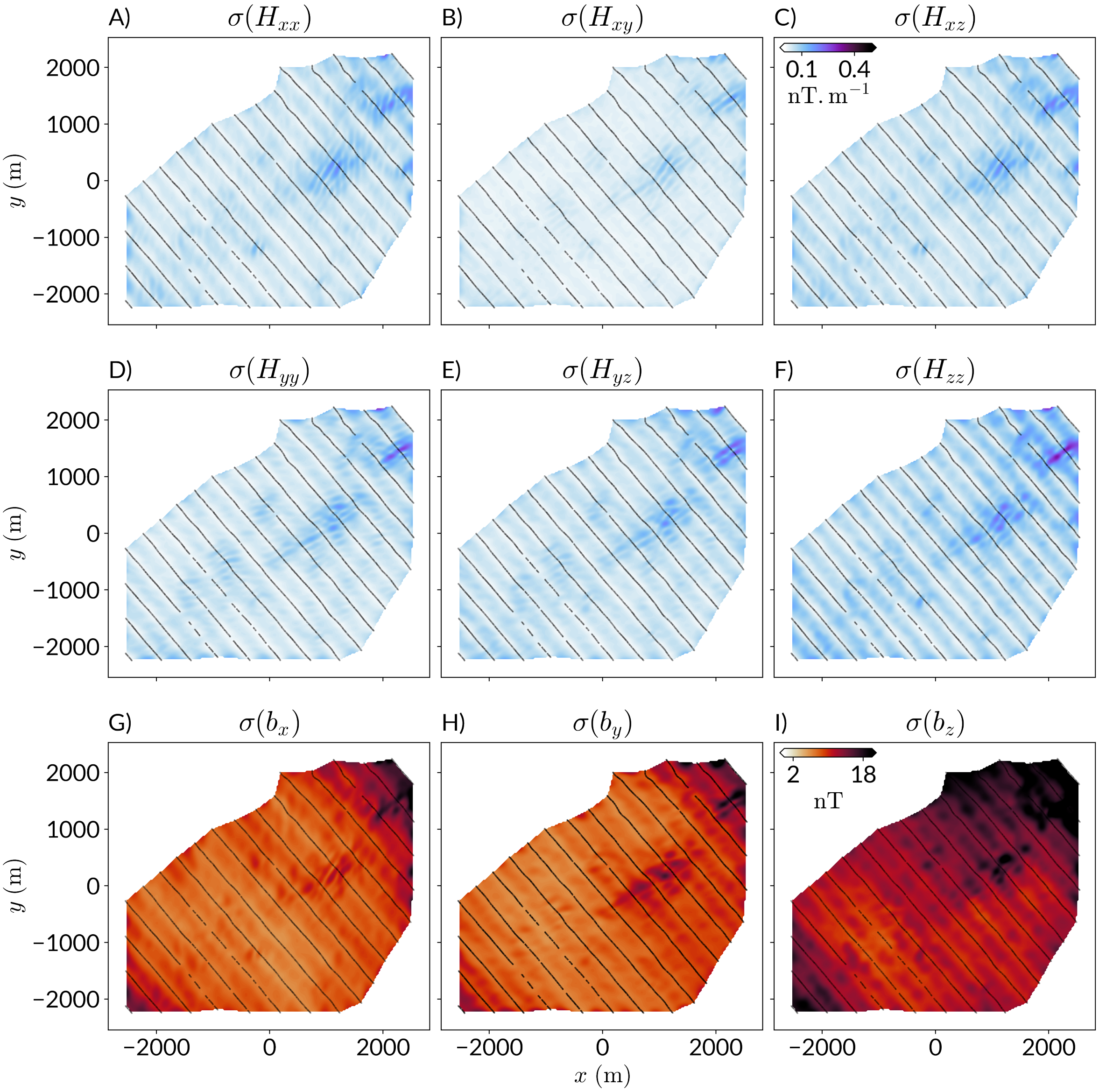

Figure 10. Uncertainty maps for the 100-model ensemble. The standard deviation computed across 100 models for the A) H_{xx}, B) H_{xy}, C) H_{xz}, D) H_{yy}, E) H_{yz}, and F) H_{zz} components, and the recovered G) b_x, H) b_y, and I) b_z vector components.